Morphology determination of luminescent carbon nanotubes by analytical super-resolution microscopy approaches

Benjamin P. Lambert[1,2], *Hadrien Kerkhof*[1,2], *Benjamin S. Flavel*[3], *Laurent Cognet*[1,2*]

[1] Laboratoire Photonique Numérique et Nanosciences, Université de Bordeaux, 33400 Talence, France

[2] LP2N, Institut d'Optique Graduate School, CNRS UMR 5298, 33400 Talence, France

[3] Institute of Nanotechnology, Karlsruhe Institute of Technology, Kaiserstraße 12, D-76131 Karlsruhe, Germany

*Correspondence: laurent.cognet@u-bordeaux.fr

Abstract

The ability to determine the precise structure of nano-objects is essential for a multitude of applications. This is particularly true of single-walled carbon nanotubes (SWCNTs), which are produced as heterogeneous samples. Current techniques used for their characterization require sophisticated instrumentation, such as atomic force microscopy (AFM), or a compromise on accuracy. In this paper, we propose to use super-resolution microscopy (SRM) to accurately determine the morphology (orientation, length and shape) of individual luminescent SWCNTs. We generate super-resolved images using three recently published SRM analytical software packages (DPR, eSRRF and MSSR) and metrologically compare their performance to determine the morphological properties of SWCNTs. For this, ground-truth information on nanotube morphologies were obtained using polarization measurements and AFM to directly correlate the results from SRM at the single particle level. We show a more than 4-fold improvement in resolution over standard photoluminescence imaging, revealing hidden morphologies as efficiently as AFM. We finally demonstrate that DPR, and eventually eSRRF, can effectively assess SWCNT length distribution in a much faster and more accessible way than AFM. We believe that this approach can be generalized to other types of luminescent nanostructures and thus become a standard for rapid and accurate characterization of samples.

Introduction

Single-walled carbon nanotubes (SWCNTs) are well known materials for applications ranging from energy and composite additives to microelectronics and biosensing[1–4]. Yet accurate characterization of their structure is fundamental for understanding and designing correctly SWCNT-based systems. This is all the more important as SWCNTs generally come in a mixture of different lengths and chiralities (diameters). While the chirality of nanotubes can reliably be determined by photoluminescence (PL) spectroscopy in the near infrared (NIR)[5], assessing their orientation, curvature and length requires more complex characterization techniques. The most common methods used to characterize the morphological attributes of SWCNTs are scanning electron microscopy, transmission electron microscopy and atomic force microscopy (AFM), as they exhibit resolutions close to or less than the nanotube diameter of around 1 nm[6]. However, these methods have a low throughput (typically a whole day is needed to analyze a few hundred nanotubes), and they require specific instrumentation and tedious sample preparation with extensive cleaning processes aimed at removing impurities (surfactants, dust, rough substrate) that would strongly affect the final image quality. Moreover, AFM does not provide information on the chirality of the observed nanotubes. Alternatively, approaches based on the optical detection of SWCNT diffusion in liquids have been proposed to determine the length of SWCNTs. They include depolarized dynamic light scattering (DDLS)[7], multiangle light scattering (MALS)[8] and length by analysis of nanotube diffusion (LAND)[9,10]. Light scattering-based approaches, such as DDLS and MALS, have the disadvantage of being poorly accurate for polydisperse samples as they provide average lengths rather than length distributions and are strongly affected by the presence of SWCNT aggregates or impurities. LAND, on the other hand, is poorly affected by the presence of impurities as it is based on the SWCNT PL in the NIR but it requires bright samples and a high-speed imaging system, as the accuracy of SWCNT length depends on the framerate (up to ca. 125 fps), and can suffer errors due to spatial drift. More importantly, all these approaches are blind measurements and only give an estimate of the length of the SWCNT population but do not inform on the actual length of each individual SWCNT. This aspect can be particularly critical in applications where

individual nanotubes are investigated such as in field effect transistors[11,12] and fundamental studies[13,14]. This is also the case for biological applications where precise determination of SWCNT arrangements inside cellular bodies could help understand better uptake mechanisms[15,16]. While AFM can be useful for this purpose for example in fixed biological samples[17], fluorescence microscopy has the advantage of being more versatile as it can provide information on SWCNT structure (length, chirality) including in live samples as well as on the chemical environment at the SWCNT surface thanks, for example, to hyperspectral imaging[18,19]. The length of individual long SWCNTs was previously assessed by fitting the intensity profiles with a formula that includes the exciton diffusion length, thus accounting for the fluorescence loss at the nanotube ends due to exciton quenching[20,21]. However, fluorescence microscopy is intrinsically limited by the diffraction of light ($\frac{1.22\lambda}{2NA} \sim \frac{\lambda}{2}$, with λ the emitter's wavelength and NA the numerical aperture of the objective) which prevents one to resolve structures smaller than the diffraction limit, around 500 nm for (6,5) nanotubes emitting at ca. 1000 nm. In this context, the NIR wavelength stands here as a penalty as compared to nanostructures emitting at shorter wavelengths.

Although unavoidable, diffraction is not a definite barrier and can be circumvented using super-resolution microscopy (SRM) approaches[22]. Near-field microscopy was first proposed to successfully resolve and study carbon nanotubes with nanometric precision[23–25], but it remains challenging, requires sophisticated equipment and has low throughputs. In the far-field, following pioneering super-resolution strategies[26], super-localization of individual excitons along a single SWCNT was achieved by fitting the position of spectrally-separated emitters at cryogenic temperatures[27]. At room temperature, the most resolutive SRM methods rely on the intermittent activation and deactivation of neighboring fluorescent emitters, either chemically or optically, allowing to isolate the contribution of each emitter and defining their resulting position with localization precision greater than the diffraction limit. The chemical route was the first used to super-resolve the structure of NIR emitting carbon nanotubes by inducing a blinking of the excitons through reversible adsorption of protons on the nanotube surface[28]. Blinking-based super-resolution imaging of carbon nanotubes was also achieved on chemically-modified carbon nanotubes using

photoswitchable molecules[29] or surface charges[30], allowing to localize the position of individual chemical moieties on the carbon nanotube surface at nanometer resolutions (down to 25 nm $\sim \frac{\lambda}{40}$). However, although effective, these strategies require specific conditions (additives, surface charges, functionalization) to induce a blinking of the emission. They also require lengthy measurements to obtain sufficiently high blinking statistics, hence the need for massive data analysis and control of nanometric drifts in optical instrumentation. Other SRM approaches which rely on non-linear behaviors of the fluorescence emitters, such as exciton-exciton annihilation[31] or stimulated-emission-depletion[32], could also be considered but they generally require intense illumination or specific and expensive instrumentation.

On the other hand, several analytical approaches have been developed for super-resolution imaging. Some approaches rely on the analysis of the intensity fluctuations from a stack of images acquired at the same location such as for the Super-resolution Optical Fluctuation Imaging[33] and Super Resolution Radial Fluctuations (SRRF[34,35]). Interestingly, the SRRF algorithm primarily calculates the degree of convergence of the local intensity gradient (i.e. radiality) at the sub-pixel level in the initial image to find the position of individual emitting point sources. Other approaches rely on image deconvolution to recover the shape of the emitting nanostructures, as in the case of Mean-Shift Super Resolution (MSSR[36]). This method is based on the local calculation of the mean shift vector throughout the image, a vector that points in the direction of the intensity gradient and whose length provides a local measure of the fluorescence brightness and density. MSSR is an iterative process meaning that a super-resolved image resulting from the analysis can be fed back into the algorithm *n* times to further improve resolution. Alternatively, the Deblurring by Pixel Reassignment (DPR[37]) involves reallocating pixel intensities to neighboring locations according to the magnitude and direction of the locally normalized image gradient. These algorithms have all been demonstrated for the super-resolution of biological structures and have shown a significant gain in resolution. According to the standard Rayleigh criterion, which defines the resolution based on the diffraction limit, resolutions as low as ca. $\frac{\lambda}{7.7}$, $\frac{\lambda}{4}$ and $\frac{\lambda}{3.6}$ were reported for the eSRRF (the "enhanced" version of the SRRF[35]), DPR and MSSR respectively[35–37]. Other analytical techniques such as Structured

Illumination Microscopy[38] or Random Illumination Microscopy[39] require specific illumination schemes and have limited resolution enhancements. Interestingly, the SRRF approach was first proposed for the super-resolution imaging of carbon nanotubes[40]. Additional work has also investigated the use of a machine-learning algorithm based on SRRF images to deconvolute diffraction-limited carbon nanotubes images[41]. However, while providing clear improvements to the fluorescence images, the images obtained in both studies exhibited some artefacts at the nanotube ends, as commonly observed in SRRF, which might affect the accuracy of nanotube orientation, shape or length determination. Overall, direct comparisons between analytical SRM approaches and with ground truth information is crucially lacking for widespread application of SWCNT super-resolution imaging.

In this article, we compare the performance of three recent super-resolution analytical approaches, eSRRF, DPR and MSSR for determining carbon nanotube morphologies. We confront the results obtained with each approach with the ground truth information delivered by polarization measurement for the nanotube orientation and AFM for nanotubes orientation and length. We demonstrate here that the DPR approach gives the best results followed by eSRRF whereas MSSR images display noticeable artefacts that can affect orientation, shape and length determination.

Results/Discussion

In this work, (6,5)-purified SWCNTs were used to enable direct comparison between fluorescence microscopy and AFM images since non-purified samples contain substantial amounts of non-emissive nanotubes, including metallic species, which would bias the comparison of nanotube length distributions analyzed by the two approaches. For fluorescence imaging, sodium deoxycholate (DOC)-suspended SWCNTs were first deposited on a glass slide by spin-coating on a thick layer of polyvinyl-pyrrolidone (PVP, see **Methods**) to avoid interaction between SWCNTs and the surface charges of the glass coverslip which could lead to blinking[42,43]. The SWCNT PL was monitored on an inverted fluorescence microscope with an 845 nm excitation enabling efficient excitation of the (6,5) SWCNTs on their K-phonon sideband as previously reported[44]. Videos of 1000 frames (100 ms per frame) were recorded over four different fields of view and subsequently analyzed by the MSSR, eSRRF and DPR routines. Indeed, although these approaches can be applied to single images, analyzing a set of images of the same object (through temporal averaging for example) allows to improve drastically the quality of the final super-resolved image. It is important to mention that each of the analytical SRM algorithms have their own specific parameters that needed to be optimized for proper analysis and fair comparison (see **Methods**). We screened all the parameters of the three algorithms by comparing the resulting images first visually (presence of artefacts), then by comparing the resolution in each condition and finally by using the Super-Resolution Quantitative Image Rating and Reporting of Error Locations (SQUIRREL) routine which gives an estimate of the accuracy of super-resolved images[45]. The SQUIRREL routine calculates the convolution of the super-resolved image with the microscope's point spread function (PSF) and compares the convoluted image with the initial diffraction-limited image. Noteworthy, all three algorithms perform initial image upscaling prior to the super-resolution analysis. For eSRRF and MSSR, images are magnified through a user-defined Fourier interpolation (4x or 10x) prior to analysis while DPR performs magnification by spline interpolation to a fixed ratio of 8.33 divided by the full-width at half maximum (FWHM) of the optical setup PSF (2.07 pixels here, so 4.02x magnification). We investigated 4x and 10x magnifications for the eSRRF and MSSR

but show only in the article the results obtained with 4x magnification as this magnification yields the best overall performances (**Figures S1, S2**).

We first compared the computer analysis time required by the different SRM algorithms to provide super-resolved images from the raw data. Using the same computer (32 GB RAM, 8-core 3.59 GHz CPU, 6 GB GPU) and a video of 1000 frames with 256x256 pixels as testing dataset, the analysis took 78 s for DPR, 327 s for eSRRF and over 24 h for MSSR processing. DPR and eSRRF analyses therefore display equivalent processing times while MSSR processing is much slower (or can be accelerated by using a more powerful computer) to achieve the same task.

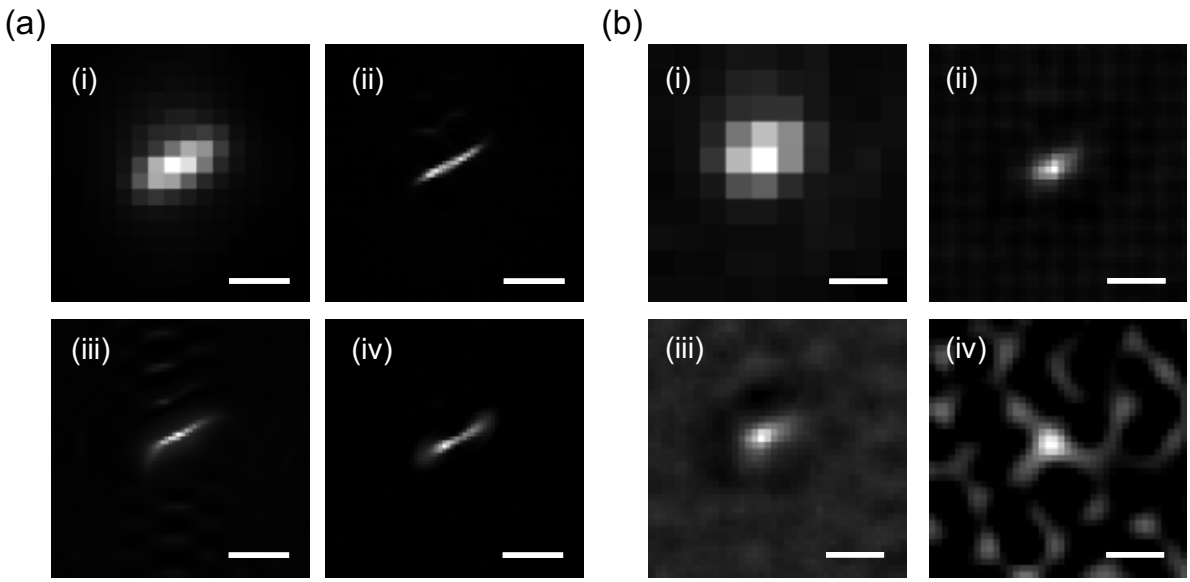

Figure 1. *Comparison of the different analytical SRM methods for the super-resolution of (a) an optically long SWCNT (scale bar: 1 µm) and (b) a diffraction limited SWCNT (scale bar: 600 nm). (i): Raw image. (ii): DPR. (iii): eSRRF. (iv): MSSR.*

For analysis, regions of interest (ROIs) were automatically created around each SWCNT found in the initial raw (diffraction-limited recorded) image and the corresponding ROIs were used in the super-resolved images. We observed mostly unresolved diffraction-limited SWCNTs (i.e. shorter than ~500 nm), but also

a few “optically long” SWCNTs were found. For these long nanotubes, their shape and orientation could thus be visually determined. By displaying the images obtained with the different SRM approaches for optically long SWCNTs (**Figure 1a**), a clear improvement of resolution can be visually observed in accordance with previous reports based on the SRRF method[40]. Careful examination of the images, however, reveals the presence of artifacts at the nanotube ends for eSRRF and MSSR images, in contrast to DPR where the nanotube ends are better defined. This observation was even more striking when analyzing diffraction-limited SWCNTs (**Figure 1b**) where it is not possible to distinguish the presence of a clear tubular structure in the eSRRF and MSSR images (due to the appearance of structural noise), whereas the DPR image more clearly reveals an elongated shape. The better performance of DPR is probably due to the fact that eSRRF and MSSR are non-linear algorithms which are therefore likely to generate artifacts in the final image such as holes in elongated structures[34,36,46]. In contrast, DPR operates linearly in the real space and thus preserves the intensities of the initial image and prevents the generation of intensity artefacts[37].

Although the DPR approach provides qualitatively better images, a quantitative comparison with the actual SWCNT morphologies is needed to state whether the obtained structures are valid. For that, we first relied on an orientation analysis that we applied on 247 individual SWCNTs. The strong polarizability of the SWCNTs along their axis[13] indeed allows to evaluate the orientation of the tubes by analyzing the polarization orientation of their PL emission. A polarized excitation was not considered because of the presence of birefringence in some optics inside the microscope, making tedious the generation of linear polarization in any direction. All excitations performed in this work were thus set to circular polarization to generate equivalent excitation efficiency regardless of nanotube orientations. To efficiently examine the linear polarization emission of each SWCNTs, we used a rotating Glan-Thompson polarizer placed in the detection path of the microscope (**Figure 2a**).

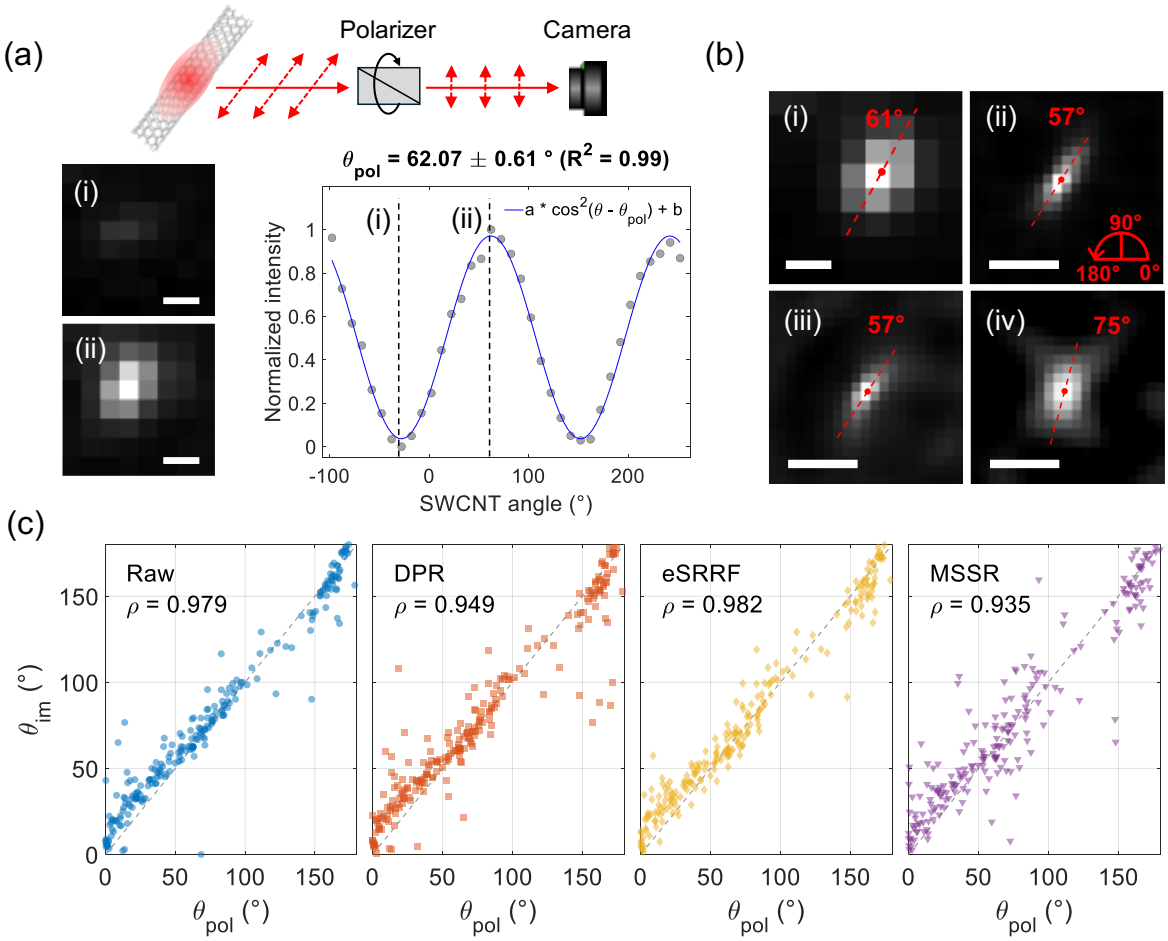

Figure 2. *Determination of SWCNT orientations. (a): Analysis of a SWCNT polarized emission allows to determine the SWCNT orientation by fitting the intensities to a Malus law. (i, ii): examples of (i) lowest and (ii) highest SWCNT intensity images. Scale bars: 500 nm. (b): Determination of the SWCNT orientation from 2D Gaussian fitting on the (i) raw, (ii) DPR, (iii) eSRRF and (iv) MSSR images recorded in the absence of the polarizer. The angles are determined from 0 to 180° in a counterclockwise direction (shown in red). The center and axis of the tubes are indicated by a red point and dotted line. Scale bars: 500 nm. (c): Comparison of the angle obtained from the 2D Gaussian fit θ_{im} as a function of the angle determined from the polarization analysis θ_{pol} for the raw (blue circles), DPR (red squares), eSRRF (yellow diamonds) and MSSR (purple triangles) images. The Pearson correlation coefficient is given in each case ($p<0.05$ for all, $n=247$ nanotubes). A grey dotted line represents the y=x perfect case.*

By analyzing the sum of the intensities in the ROI for each angle θ of the polarizer (from 0 to 360°), it is possible to determine the angle θ_{pol} of the SWCNT by fitting the obtained values to a Malus law:

$$a * \cos^2(\theta - \theta_{pol}) + b \quad (1)$$

with a, b adjusting constants. Note that for this analysis, only straight nanotubes were analyzed to provide unambiguous angle orientations.

Images of SWCNTs in raw and super-resolved images were fit to a 2D asymmetric Gaussian function to retrieve the apparent nanotube orientation θ_{im} in each image (**Figure 2b**). The retrieved orientations θ_{im} were then plotted against to the (true) orientations θ_{pol} determined from polarization analysis and the similarity of the two angles was evaluated by Pearson's correlation analysis (**Figure 2c**). We found good correlation ($\rho > 0.9$) for all cases, including the diffraction limited images, which indicates that a 2D Gaussian fit is already adequate to evaluate nanotube orientation without requiring the super-resolution of the SWCNTs. This statement cannot be universal e.g. for nanotubes significantly shorter than the diffraction limit, and should thus depend on the length distribution of the nanotubes. We observed a slightly larger spread of the orientation values for the MSSR analysis, indicating that the artefacts generated by this approach, as mentioned above (**Figure 2b**), bias the orientation determination.

This analysis confirmed that nanotube orientations retrieved from SRM images accurately describe the organization of the SWCNTs on the sample. Encouraged by these results, a more in-depth analysis was carried out by performing correlative imaging between fluorescence microscopy and AFM to give access to the ground truth length, orientation and bends of the nanotubes. For this, SWCNTs were immobilized on a gridded cover glass using poly-l-lysine (PLL, see **Methods**) and thoroughly washed to avoid the presence of impurities on the surface. In order to register the PL images on the AFM images, we recorded brightfield images at the same location as the PL images (with the same camera) and compared the position of the grid between the brightfield and AFM images (**Figure S4**).

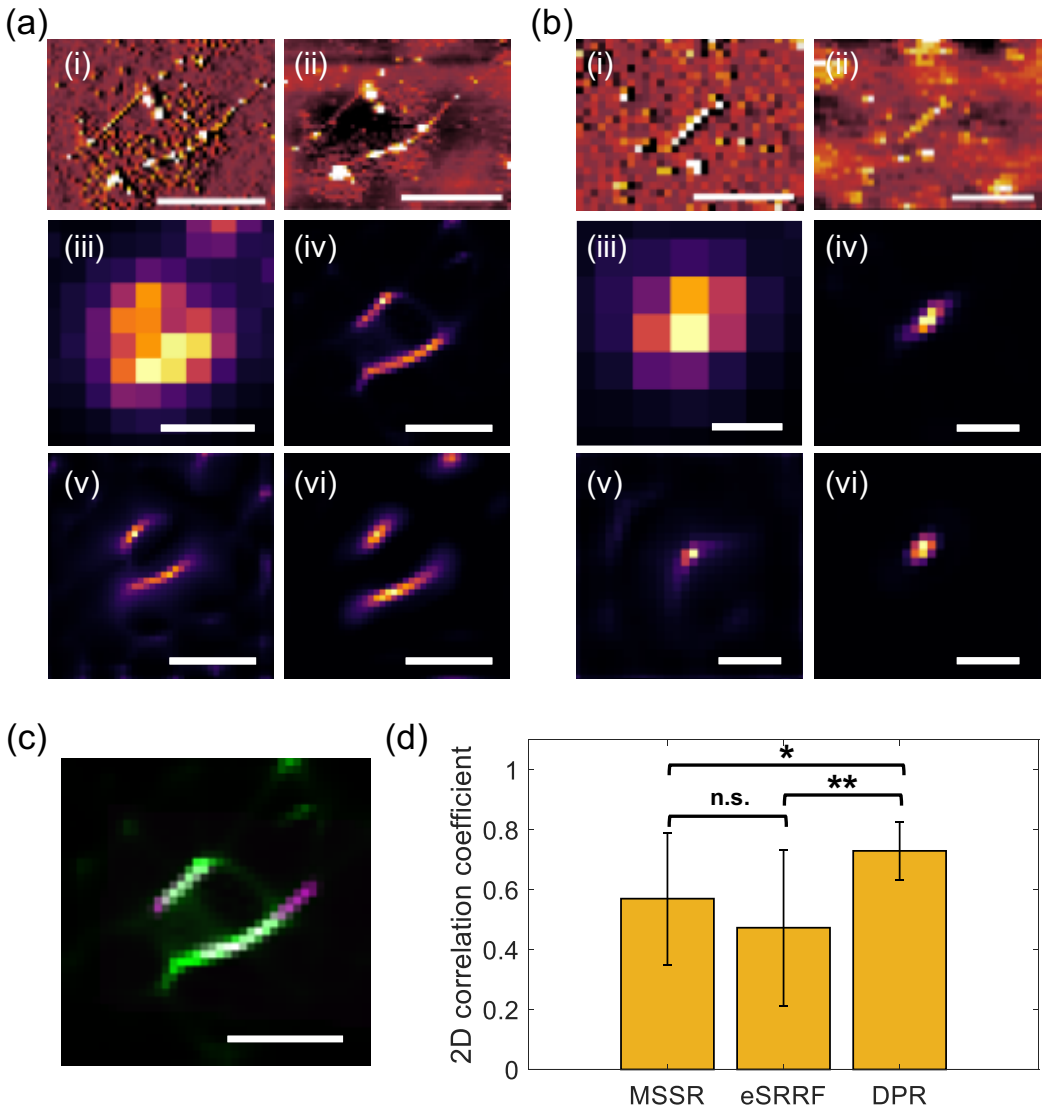

Figure 3. *Correlative measurement of SWCNT morphologies between AFM and fluorescence microscopy for (a) two closely located SWCNTs (scale bars: 1 µm) and (b) a diffraction limited SWCNT (scale bars: 500 nm). Panels in (a,b) correspond to: (i) amplitude AFM image, (ii) height AFM image, (iii) raw PL image, (iv) DPR image, (v) eSRRF image, (vi) MSSR image. (c): Registered combined image of the AFM-based skeletonized SWCNT shape (pink) and the DPR PL image (green). Scale bar: 1 µm. (d): 2D correlation coefficient between the AFM-based skeletonized SWCNT shape and the SRM images for MSSR, SRRF and DPR (mean ± standard deviation on 10 images). Two sample t-tests were calculated between the MSSR and eSRRF (n.s., p=0.38), DPR and MSSR (*, p<0.05), DPR and eSRRF (**, p<0.01) categories.*

Visually, a better correspondence with AFM images was again found for the DPR images, whether when two closely located or a diffraction limited SWCNT are imaged (**Figure 3a,b**). DPR images indeed resulted in more defined nanotube ends and shape. To quantify this observation, a manual skeletonization of the SWCNT shapes found in AFM was performed (**Figure S6**), followed by registration with the PL super-resolved image and the calculation of the 2D correlation coefficient between the two images (**Figure 3c,d** and **Figure S7**). Interestingly, SRM images showed sometimes deviations from the AFM structures, particularly at the ends of the nanotubes, which we attribute mainly to exciton quenching at the nanotube ends or possibly to the presence of quenching species on the nanotube surface. DPR unambiguously provides an excellent correspondence with the AFM measurement, exhibiting a significantly higher ($p<0.05$, two sample t-test) correlation coefficient of 0.73 ± 0.09, as compared to MSSR (0.57 ± 0.22) and eSRRF (0.47 ± 0.26) which are equally less efficient for this objective ($p=0.38$, two sample t-test). We also noticed that, for some short nanotubes, eSRRF analysis resulted in a blank image while DPR and MSSR were able to generate super-resolved images of the nanotube (**Figure S7**). These results also confirm that analytical SRM approaches, in particular DPR, can be used effectively to analyze both straight and curved SWCNTs.

Finally, we investigated whether the super-resolved images can be used to accurately determine the length distribution of a SWCNT preparation. To this aim, we plotted the signal intensities along the nanotube axis of 247 nanotubes (**Figure 4a**), defined by the orientation of the nanotube measured above. Crochet et al.[20] showed that the length of a SWCNT could be retrieved from its luminescence image by fitting the PL intensities along its axis using the following equation:

$$c(x) = \left[1 - \frac{\sinh\left(\frac{x}{l_D}\right) + \sinh\left[\frac{L-x}{l_D}\right]}{\sinh\left(\frac{L}{l_D}\right)}\right] \quad (2)$$

with l_D the exciton diffusion length, typically between 100 and 300 nm depending on the surfactant[47,48], and L the length of the nanotube.

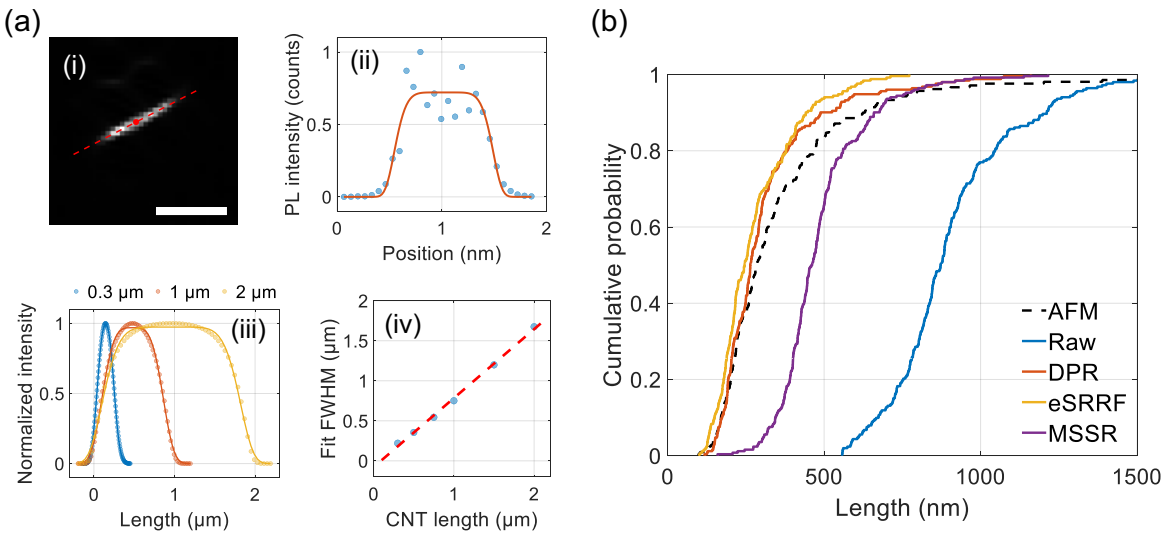

Figure 4. *Determination of SWCNT lengths. (a): Methodology used for the determination of SWCNT length from SRM images. Fitting of (i) SWCNT intensity profiles along the tube axis (scale bar: 1 µm) by (ii) the super-Gaussian function (blue points: data, red line: fit). (iii): Example of simulated intensity profile curves (points) for three different nanotube lengths (blue: 300nm, red: 1000 nm, yellow: 2000 nm) and fitted with super-Gaussian curves (solid lines). (iv): Calibration curve of the fitted FWHM as a function of nanotube length (points: simulated data, dotted line: linear fit). (b): Cumulative distributions of SWCNT lengths measured by AFM (black dotted) or extracted from the raw (blue), DPR (red), eSRRF (yellow) and MSSR (purple) images (n=247 nanotubes).*

In practice, this analysis requires micrometer long nanotubes as this fitting function fails to converge when nanotube images only display a few data points in their central part. Short SWCNT PL intensity profiles are indeed closer to a Gaussian profile (**Figure 4**, **Figure S8**). To overcome this difficulty, we introduced the use of a phenomenological fitting function in the form of a super-Gaussian:

$$c(x) = a * exp\left[-\ln(2) * \left(4\frac{(x-\mu)^2}{w^2}\right)^b\right] \quad (3)$$

with a, b adjustment constants, µ and w the center and FWHM of the super-Gaussian, respectively. This function is highly versatile as it enables fitting both Gaussian-like (i.e. short SWCNTs) and flat top-like

curves (i.e. long SWCNTs) as can be shown in **Figures S8-9**. To obtain the true SWCNT length from the FWHM given by the super-Gaussian fit, we created a reference curve from intensity profiles generated from equation (2) with defined lengths L, and fitting these profiles by the super-Gaussian function. The intensity profiles were created for an exciton diffusion length of 200 nm (the value found for (6,5) nanotubes coated with 1% DOC[20]), nanotube lengths ranging from 300 to 2000 nm and were convoluted with the PSF of the imaging modality at each nanotube ends (x=0 and L). The PSFs to consider for each case (raw data, DPR, eSRRF, and MSSR) were measured on experimental images of the 247 nanotubes studied by fitting transverse cross-section of each nanotube image with a Gaussian curve. Reference curves were then used to extract experimental SWCNT lengths from the fitted FWHM values. The resulting SWCNT length distributions are plotted in **Figure 4b**. A very close agreement is found between the lengths measured by AFM (median: 284 nm) and the length determined by both DPR (median: 264 nm) and eSRRF (median: 246 nm) images. Interestingly, DPR tend to better reveal the presence of the longer tubes of the distribution (≥420nm) than eSRRF, probably due to the non-linear treatment of eSRRF which does not preserve the fidelity of image intensity (**Figure 1**). On the other hand, MSSR resulted in an overestimation of SWCNT lengths (median: 460 nm) that we attribute to the lower resolution achieved with this technique, resulting in a larger PSF (up to twice greater as compared to DPR in the most extreme cases, see **Figure S12**). Finally, as expected, the raw images greatly overestimated the SWCNT lengths (median: 872 nm) demonstrating here the power of super-resolution in the determination of SWCNT lengths.

Overall, thanks to the versatility of fluorescence microscopy as well as the ease and speed of sample preparation and analysis, we are confident that analytical SRM strategies, in particular DPR, will become a serious alternative to the state-of-the-art approaches used today for characterizing carbon nanotube samples. Nonetheless, one should stress that analytical SRM approaches still exhibit limited resolutions that cannot yet compete with the resolutions attained by some other SRM approaches such as single-molecule localization microscopy methods[49]. We believe that the situation may evolve rapidly through, for instance, the help of machine learning tools. Other future improvements could also be oriented towards the

development and use of analytical SRM solutions working in a single frame[50] to allow, for example, to super-resolve nanostructures in motion.

Conclusions

In this paper, we metrologically compared three super-resolution analytical approaches for their ability to provide accurate estimates of luminescent carbon nanotube morphologies. The DPR, eSRRF and MSSR methods were investigated and benchmarked on identical datasets. We propose a rigorous analysis to automatically and efficiently process the images created by each of these SRM approaches over hundreds of tubes with varying orientation, shapes and lengths. Importantly, the results obtained by SRM were critically compared to the ground truth morphologies of the nanotubes in the sample by performing polarization and AFM measurements. While all three SRM approaches improved qualitatively the appearance of SWCNT structures, with resolution of ~100 nm to be compared to the theoretical diffraction limit of 414 nm (for a nanotube emission at 985 nm, **Figure S11**), DPR exhibited the best results by a significant margin due to the absence of noticeable artifacts induced by the image processing. Strikingly, SWCNT structures revealed by DPR images were very close to the structures measured by AFM at the single nanotube level, both in terms of nanotube shape and length. We therefore propose DPR, combined with our analysis routine based on a simple fitting procedure, as a fast, easy and efficient alternative to AFM for the measurement of the length distributions as well as morphologies of SWCNT samples at the single particle level. More generally, analytical SRM approaches, such as DPR (or eSRRF) should find numerous applications for the characterization of luminescent nanostructures at the single particle level.

Methods/Experimental

Sample preparation

Unless otherwise specified, the chemicals used were purchased from Sigma Aldrich.

Carbon nanotubes used in this study are (6,5) nanotubes in 1% (w/w) DOC sorted by aqueous two-phase extraction from SG65i CoMoCAT SWCNTs following a previously published approach[51].

For the fluorescence microscopy experiments, the glass slides were cleaned by subsequent bath sonication steps in acetone, isopropanol and water for 10 minutes each, followed by plasma cleaning for 2 minutes at 180 W (Atto, Diener), spin coated with 3 layers of 3% (w/w) PVP (100 µL, 4000 rpm 30 s) followed by a spin coating (Spin150i, Polos) of the carbon nanotube solution (50 µL, 4000 rpm 30 s, $C=6.5x10^{-2}$ $mg.L^{-1}$ using $\varepsilon_{E11}=0.2$ $L.mg^{-1}.cm^{-1}$ [52]).

For the AFM-microscopy correlative experiments, gridded glass slides (grid-50, Ibidi) were first cleaned with an alkaline solution (Helmanex III) at 60°C for 1h to passivate the surface and remove glass debris from the surface for the AFM measurements and subsequently plasma cleaned for 2 minutes at 180 W. The cleaned coverslips were then coated with poly-L-lysine (PLL, 100 µL, 0.01% (w/w)) for 1h, washed 2 times with deionized (DI) water, then incubated with carbon nanotubes (50 µL drop deposited on the surface, $C=6.5x10^{-3}$ $mg.L^{-1}$) for 1h and followed by 2 washes with DI water and dried over 48h at 50°C.

For the AFM measurement of nanotube lengths, mica (muscovite mica, Sigma Aldrich) was freshly exfoliated with tape, followed by a spin coating of the carbon nanotubes (50 µL, 4000 rpm 30 s, $C=6.5x10^{-2}$ $mg.L^{-1}$) and air dried overnight at room temperature.

Fluorescence microscopy measurements

The measurements were performed on an inverted microscope (Nikon Ti2) equipped with an EMCCD camera (ProEM HS 512x512, Princeton Instruments), an 845 nm laser excitation (LaserBoxx LBX-850, Oxxius) and a 60X objective (Plan Apo TIRF, NA=1.45, oil immersion, Nikon). A 900 nm longpass dichroic mirror (DMLP900R, Thorlabs) was used in combination with a 950 nm longpass filter (FELH0950, Thorlabs) in order to select the emission of the (6,5) nanotubes around 984 nm. A 256x256 ROI centered on the center of the sensor was selected for the measurements with an exposure time of 100 ms and an electron-multiplying gain of 100.

For the polarization experiments, a Glan-Thompson polarizer (GTH10M, Thorlabs) was positioned in the detection path of the fluorescence microscope in front of the camera on a rotating mount in order to visualize the polarized emission of individual carbon nanotubes.

For the AFM-microscopy correlative experiments, the grid pattern was imaged in brightfield and the SWCNT PL was recorded as described above but using the full sensor area of the camera (512x512 pixels).

AFM measurements

The measurements were performed with an AC160TS tip (Olympus, N=11.16-31.72 N/m, f=221.1-322.0 kHz). For the length measurements, images were recorded at a scan rate of 0.7 Hz and pixel size of 29.3 nm (15x15 µm area). For the correlative imaging measurements, on each field of view a large area (40x40 µm, pixel size: 78.1 nm, scan rate: 0.2 Hz) was first recorded to locate the position of the nanotubes with respect to the grid and smaller areas (20x20 µm, pixel size: 39 nm, scan rate: 0.4 Hz) were recorded within the previous image to have a more resolved image of the individual nanotubes.

Optimization of the analytical SRM parameters

The eSRRF and MSSR routines were ran on FIJI 1.54f. The DPR routine was ran on Matlab R2022a. The 3 SRM approaches require specific input parameters: amplification (final magnification), number of images to take in account for the analysis, temporal analysis approach (average and variance mostly for MSSR and

eSRRF), mesh grid analysis (bicubic or Fourier for MSSR), estimated size of the PSF (for DPR and MSSR), radius of the local-minimum filter (for DPR), gain (for DPR), sensitivity (for eSRRF). In this work, we fixed the following parameters based on SQUIRREL analysis combined with visual analysis (artefacts minimization) and minimization of the final resolution (FWHM of a Gaussian fit applied to the transverse cross section of an optically-long nanotube):

_eSRRF: 10x or 4x amplification, radius: 0.5, sensitivity: 2, 1000 frames average projection

_MSSR: 10x or 4x magnification, 2.07 pixels wide PSF, Fourier mesh grid, order 1, 1000 frames average projection

_DPR: high resolution magnification (gain 2), 2.07 pixels wide PSF, 35.19 used for the radius of the local-minimum filter, 1000 frames average projection

Orientation determination analysis

The diffraction limited and SRM images were analyzed on Matlab R2022a. The positions of each carbon nanotube were determined by a custom 2D Gaussian fitting algorithm (Levenberg-Marquardt "levmar" nonlinear least squares optimization[53]). ROIs of 10x10 pixels (for the diffraction limited images), 40x40 pixels (for the SRM images with 4x amplification) and 100x100 pixels (for the SRM images with 10x amplification) were created around each detected nanotube. For each ROI, the center and the orientation of the 2D Gaussian fit were determined and plotted.

The images obtained after the polarizer exhibited a circular drift as a function of polarizer angle and were thus registered so that the nanotube would exhibit the same position as in the diffraction limited image without polarizer using the imregister function in Matlab. The polarized images were then analyzed using the same ROIs created in the previous step. The sum of the ROI was calculated for each angle of the polarizer, from 0 to 360 degrees every 10 degrees, and plotted as a function of the polarizer angle. The resulting curves were fitted with a Malus law (equation (1)). In order to calibrate the nanotube orientation

with respect to the polarizer angles, we selected an optically long carbon nanotube whose orientation could be determined accurately from the diffraction-limited image using the 2D Gaussian fitting algorithm (**Figure S3**), associated this angle value to the value determined with the fit of the polarizer angles and then propagated this calibration to all the other carbon nanotubes. Because the orientation was determined using a 2D Gaussian fit, we only included straight nanotubes and excluded those having curved shapes.

Shape determination analysis

The AFM images were analyzed using the Gwyddion software and were exported to 16-bit images. The selected nanotubes all exhibited a height around 1-2 nm consistent with the expected diameter of a surfactant-coated nanotube[54] (**Figure S5**). The shape of each selected nanotube was then analyzed in FiJi by manually drawing the nanotube structure and exporting the resulting skeletonized selection as a binary image for further analysis.

In order to find the same nanotubes in both AFM and fluorescence microscopy, we used reference points in the images using both the reference grid of the coverglass (letters, numbers and lines) and impurities on the substrate (dust particles, aggregates) as shown in **Figure S4**.

To overlap the fluorescence SRM images and the AFM skeletonized structures, we resized the AFM images to match the pixel size of the SRM images and registered both images using the imregister function in Matlab. We then ran a calculation of the 2D correlation coefficient (corr2 function in Matlab) for the registered fluorescence-AFM image couples.

Length determination analysis

The physical length of the nanotubes was determined using AFM. The AFM images were converted to 16-bits images and analyzed in FIJI by using a pixel size of 39 nm. The lengths of the nanotubes were measured by hand-drawing straight or segmented lines (depending on the nanotube shape).

Acknowledgements

This work was performed with financial support from CNRS, the University of Bordeaux, the France-BioImaging National Infrastructure (ANR-10-INBS-04-01), and the European Research Council Synergy grant (951294) to LC; LC also acknowledges support from the EUR Light S&T (PIA3 Program, ANR-17-EURE-0027) and the Idex Bordeaux (Grand Research Program GPR LIGHT); BL acknowledges funding from the European Union's Horizon 2020 research and innovation programme under the Marie Skłodowska-Curie grant agreement No. 101107105.

Abbreviations

SWCNT, single-walled carbon nanotube ; AFM, atomic force microscopy ; SRM, super-resolution microscopy ; DPR, Deblurring by Pixel Reassignment ; (e)SRRF, (enhanced) Super-Resolution Radial Fluctuations ; MSSR, Mean-Shift Super Resolution ; PL, photoluminescence ; NIR, near infrared ; DDLS, depolarized dynamic light scattering ; MALS, multiangle light scattering ; LAND, length by analysis of nanotube diffusion ; Super-Resolution Quantitative Image Rating and Reporting of Error Locations ; PSF, point spread function ; ROI, region of interest ; FWHM, full-width at half maximum ; DOC, sodium deoxycholate ; PVP, polyvinyl-pyrrolidone ; PLL, poly-l-lysine

References

(1) Maheswaran, R.; Shanmugavel, B. P. A Critical Review of the Role of Carbon Nanotubes in the Progress of Next-Generation Electronic Applications. *J. Electron. Mater.* **2022**, *51* (6), 2786–2800. https://doi.org/10.1007/s11664-022-09516-8.

(2) Ali, Z.; Yaqoob, S.; Yu, J.; D'Amore, A. Critical Review on the Characterization, Preparation, and Enhanced Mechanical, Thermal, and Electrical Properties of Carbon Nanotubes and Their Hybrid Filler Polymer Composites for Various Applications. *Compos. Part C Open Access* **2024**, *13*

(January), 100434. https://doi.org/10.1016/j.jcomc.2024.100434.

(3) Ferrier, D. C.; Honeychurch, K. C. Carbon Nanotube (CNT)-Based Biosensors. *Biosensors* **2021**, *11* (12), 1–33. https://doi.org/10.3390/bios11120486.

(4) Ackermann, J.; Metternich, J. T.; Herbertz, S.; Kruss, S. Biosensing with Fluorescent Carbon Nanotubes. *Angew. Chemie - Int. Ed.* **2022**, *61* (18). https://doi.org/10.1002/anie.202112372.

(5) Weisman, R. B.; Bachilo, S. M. Dependence of Optical Transition Energies on Structure for Single-Walled Carbon Nanotubes in Aqueous Suspension : An Empirical Kataura Plot. *Nano Lett.* **2003**, *3* (9), 1235–1238. https://doi.org/10.1021/nl034428i.

(6) Herrero-Latorre, C.; Álvarez-Méndez, J.; Barciela-García, J.; García-Martín, S.; Peña-Crecente, R. M. Characterization of Carbon Nanotubes and Analytical Methods for Their Determination in Environmental and Biological Samples: A Review. *Anal. Chim. Acta* **2015**, *853* (1), 77–94. https://doi.org/10.1016/j.aca.2014.10.008.

(7) Badaire, S.; Poulin, P.; Maugey, M.; Zakri, C. In Situ Measurements of Nanotube Dimensions in Suspensions by Depolarized Dynamic Light Scattering. *Langmuir* **2004**, *20* (24), 10367–10370. https://doi.org/10.1021/la049096r.

(8) Shetty, A. M.; Wilkins, G. M. H.; Nanda, J.; Solomon, M. J. Multiangle Depolarized Dynamic Light Scattering of Short Functionalized Single-Walled Carbon Nanotubes. *J. Phys. Chem. C* **2009**, *113* (17), 7129–7133. https://doi.org/10.1021/jp900731q.

(9) Streit, J. K.; Bachilo, S. M.; Naumov, A. V.; Khripin, C.; Zheng, M.; Weisman, R. B. Measuring Single-Walled Carbon Nanotube Length Distributions from Diffusional Trajectories. *ACS Nano* **2012**, *6* (9), 8424–8431. https://doi.org/10.1021/nn3032744.

(10) Lee, A.; Cognet, L. Length Measurement of Single-Walled Carbon Nanotubes from Translational

Diffusion and Intensity Fluctuations. *J. Appl. Phys.* **2020**, *128* (22), 224301. https://doi.org/10.1063/5.0031194.

(11) Li, J.; Zhang, Q.; Yang, D.; Tian, J. Fabrication of Carbon Nanotube Field Effect Transistors by AC Dielectrophoresis Method. *Carbon N. Y.* **2004**, *42* (11), 2263–2267. https://doi.org/10.1016/j.carbon.2004.05.002.

(12) Kamaei, S.; Saeidi, A.; Jazaeri, F.; Rassekh, A.; Oliva, N.; Cavalieri, M.; Lambert, B.; Ionescu, A. M. An Experimental Study on Mixed-Dimensional 1D-2D van Der Waals Single-Walled Carbon Nanotube-WSe2 Hetero-Junction. *IEEE Electron Device Lett.* **2020**, *41* (4), 645–648. https://doi.org/10.1109/LED.2020.2974400.

(13) Tsyboulski, D. A.; Bachilo, S. M.; Weisman, R. B. Versatile Visualization of Individual Single-Walled Carbon Nanotubes with near-Infrared Fluorescence Microscopy. *Nano Lett.* **2005**, *5* (5), 975–979. https://doi.org/10.1021/nl050366f.

(14) Fakhri, N.; Tsyboulski, D. A.; Cognet, L.; Bruce Weisman, R.; Pasquali, M. Diameter-Dependent Bending Dynamics of Single-Walled Carbon Nanotubes in Liquids. *Proc. Natl. Acad. Sci. U. S. A.* **2009**, *106* (34), 14219–14223. https://doi.org/10.1073/pnas.0904148106.

(15) Gravely, M.; Kindopp, A.; Hubert, L.; Card, M.; Nadeem, A.; Miller, C.; Roxbury, D. Aggregation Reduces Subcellular Localization and Cytotoxicity of Single-Walled Carbon Nanotubes. *ACS Appl. Mater. Interfaces* **2022**, *14* (17), 19168–19177. https://doi.org/10.1021/acsami.2c02238.

(16) Antonucci, A.; Reggente, M.; Roullier, C.; Gillen, A. J.; Schuergers, N.; Zubkovs, V.; Lambert, B. P.; Mouhib, M.; Carata, E.; Dini, L.; Boghossian, A. A. Carbon Nanotube Uptake in Cyanobacteria for Near-Infrared Imaging and Enhanced Bioelectricity Generation in Living Photovoltaics. *Nat. Nanotechnol.* **2022**, *17* (10), 1111–1119. https://doi.org/10.1038/s41565-022-01198-x.

(17) Lamprecht, C.; Liashkovich, I.; Neves, V.; Danzberger, J.; Heister, E.; Rangl, M.; Coley, H. M.; McFadden, J.; Flahaut, E.; Gruber, H. J.; Hinterdorfer, P.; Kienberger, F.; Ebner, A. AFM Imaging of Functionalized Carbon Nanotubes on Biological Membranes. *Nanotechnology* **2009**, *20* (43). https://doi.org/10.1088/0957-4484/20/43/434001.

(18) Jena, P. V.; Gravely, M.; Cupo, C.; Safaee, M. M.; Roxbury, D.; Heller, D. A. Hyperspectral Counting of Multiplexed Nanoparticle Emitters in Single Cells and Organelles. *ACS Nano* **2022**, *16* (2), 3092–3104. https://doi.org/10.1021/acsnano.1c10708.

(19) Erkens, M.; Wenseleers, W.; López Carrillo, M. Á.; Botka, B.; Zahiri, Z.; Duque, J. G.; Cambré, S. Hyperspectral Detection of the Fluorescence Shift between Chirality-Sorted Empty and Water-Filled Single-Wall Carbon Nanotube Enantiomers. *ACS Nano* **2024**, *18* (22), 14532–14545. https://doi.org/10.1021/acsnano.4c02226.

(20) Crochet, J. J.; Duque, J. G.; Werner, J. H.; Lounis, B.; Cognet, L.; Doorn, S. K. Disorder Limited Exciton Transport in Colloidal Single-Wall Carbon Nanotubes. *Nano Lett.* **2012**, *12* (10), 5091–5096. https://doi.org/10.1021/nl301739d.

(21) Oudjedi, L.; Parra-Vasquez, A. N. G.; Godin, A. G.; Cognet, L.; Lounis, B. Metrological Investigation of the (6,5) Carbon Nanotube Absorption Cross Section. *J. Phys. Chem. Lett.* **2013**, *4* (9), 1460–1464. https://doi.org/10.1021/jz4003372.

(22) Godin, A. G.; Varela, J. A.; Gao, Z.; Danné, N.; Dupuis, J. P.; Lounis, B.; Groc, L.; Cognet, L. Single-Nanotube Tracking Reveals the Nanoscale Organization of the Extracellular Space in the Live Brain. *Nat. Nanotechnol.* **2017**, *12* (3), 238–243. https://doi.org/10.1038/nnano.2016.248.

(23) Hartschuh, A.; Sánchez, E. J.; Xie, X. S.; Novotny, L. High-Resolution Near-Field Raman Microscopy of Single-Walled Carbon Nanotubes. *Phys. Rev. Lett.* **2003**, *90* (9), 4. https://doi.org/10.1103/PhysRevLett.90.095503.

(24) Hartschuh, A.; Qian, H.; Meixner, A. J.; Anderson, N.; Novotny, L. Nanoscale Optical Imaging of Single-Walled Carbon Nanotubes. *Nano Lett.* **2005**, *5* (11), 2310–2313. https://doi.org/10.1016/j.jlumin.2005.12.031.

(25) Ma, X.; Liu, Q.; Yu, N.; Xu, D.; Kim, S.; Liu, Z.; Jiang, K.; Wong, B. M.; Yan, R.; Liu, M. 6 Nm Super-Resolution Optical Transmission and Scattering Spectroscopic Imaging of Carbon Nanotubes Using a Nanometer-Scale White Light Source. *Nat. Commun.* **2021**, *12* (1), 1–7. https://doi.org/10.1038/s41467-021-27216-5.

(26) Van Oijen, A. M.; Köhler, J.; Schmidt, J.; Müller, M.; Brakenhoff, G. J. 3-Dimensional Super-Resolution by Spectrally Selective Imaging. *Chem. Phys. Lett.* **1998**, *292* (1–2), 183–187. https://doi.org/10.1016/S0009-2614(98)00673-3.

(27) Raynaud, C.; Claude, T.; Borel, A.; Amara, M. R.; Graf, A.; Zaumseil, J.; Lauret, J. S.; Chassagneux, Y.; Voisin, C. Superlocalization of Excitons in Carbon Nanotubes at Cryogenic Temperature. *Nano Lett.* **2019**, *19* (10), 7210–7216. https://doi.org/10.1021/acs.nanolett.9b02816.

(28) Cognet, L.; Tsyboulski, D. A.; Weisman, R. B. Subdiffraction Far-Field Imaging of Luminescent Single-Walled Carbon Nanotubes. *Nano Lett.* **2008**, *8* (2), 749–753. https://doi.org/10.1021/nl0725300.

(29) Godin, A. G.; Setaro, A.; Gandil, M.; Haag, R.; Adeli, M.; Reich, S.; Cognet, L. Photoswitchable Single-Walled Carbon Nanotubes for Super-Resolution Microscopy in the near-Infrared. *Sci. Adv.* **2019**, *5* (9), 1–23. https://doi.org/10.1126/sciadv.aax1166.

(30) Danné, N.; Kim, M.; Godin, A. G.; Kwon, H.; Gao, Z.; Wu, X.; Hartmann, N. F.; Doorn, S. K.; Lounis, B.; Wang, Y.; Cognet, L. Ultrashort Carbon Nanotubes That Fluoresce Brightly in the Near-Infrared. *ACS Nano* **2018**, *12* (6), 6059–6065. https://doi.org/10.1021/acsnano.8b02307.

(31) Otsuka, K.; Ishii, A.; Kato, Y. K. Super-Resolution Fluorescence Imaging of Carbon Nanotubes Using a Nonlinear Excitonic Process. *Opt. Express* **2019**, *27* (13), 17463. https://doi.org/10.1364/oe.27.017463.

(32) Blom, H.; Widengren, J. Stimulated Emission Depletion Microscopy. *Chem. Rev.* **2017**, *117* (11), 7377–7427. https://doi.org/10.1021/acs.chemrev.6b00653.

(33) Dertinger, T.; Colyera, R.; Iyer, G.; Weiss, S.; Enderlein, J. Fast, Background-Free, 3D Super-Resolution Optical Fluctuation Imaging (SOFI). *Proc. Natl. Acad. Sci. U. S. A.* **2009**, *106* (52), 22287–22292. https://doi.org/10.1073/pnas.0907866106.

(34) Gustafsson, N.; Culley, S.; Ashdown, G.; Owen, D. M.; Pereira, P. M.; Henriques, R. Fast Live-Cell Conventional Fluorophore Nanoscopy with ImageJ through Super-Resolution Radial Fluctuations. *Nat. Commun.* **2016**, *7*, 1–9. https://doi.org/10.1038/ncomms12471.

(35) Laine, R. F.; Heil, H. S.; Coelho, S.; Nixon-Abell, J.; Jimenez, A.; Wiesner, T.; Martínez, D.; Galgani, T.; Régnier, L.; Stubb, A.; Follain, G.; Webster, S.; Goyette, J.; Dauphin, A.; Salles, A.; Culley, S.; Jacquemet, G.; Hajj, B.; Leterrier, C.; Henriques, R. High-Fidelity 3D Live-Cell Nanoscopy through Data-Driven Enhanced Super-Resolution Radial Fluctuation. *Nat. Methods* **2023**, *20* (12), 1949–1956. https://doi.org/10.1038/s41592-023-02057-w.

(36) Torres-García, E.; Pinto-Cámara, R.; Linares, A.; Martínez, D.; Abonza, V.; Brito-Alarcón, E.; Calcines-Cruz, C.; Valdés-Galindo, G.; Torres, D.; Jabloñski, M.; Torres-Martínez, H. H.; Martínez, J. L.; Hernández, H. O.; Ocelotl-Oviedo, J. P.; Garcés, Y.; Barchi, M.; D'Antuono, R.; Bošković, A.; Dubrovsky, J. G.; Darszon, A.; Buffone, M. G.; Morales, R. R.; Rendon-Mancha, J. M.; Wood, C. D.; Hernández-García, A.; Krapf, D.; Crevenna, Á. H.; Guerrero, A. Extending Resolution within a Single Imaging Frame. *Nat. Commun.* **2022**, *13* (1), 1–22. https://doi.org/10.1038/s41467-022-34693-9.

(37) Zhao, B.; Mertz, J. Resolution Enhancement with Deblurring by Pixel Reassignment. *Adv. Photonics* **2023**, *5* (6), 1–28. https://doi.org/10.1117/1.AP.5.6.066004.

(38) Heintzmann, R.; Huser, T. Super-Resolution Structured Illumination Microscopy. *Chem. Rev.* **2017**, *117* (23), 13890–13908. https://doi.org/10.1021/acs.chemrev.7b00218.

(39) Mangeat, T.; Labouesse, S.; Allain, M.; Negash, A.; Martin, E.; Guénolé, A.; Poincloux, R.; Estibal, C.; Bouissou, A.; Cantaloube, S.; Vega, E.; Li, T.; Rouvière, C.; Allart, S.; Keller, D.; Debarnot, V.; Wang, X. B.; Michaux, G.; Pinot, M.; Le Borgne, R.; Tournier, S.; Suzanne, M.; Idier, J.; Sentenac, A. Super-Resolved Live-Cell Imaging Using Random Illumination Microscopy. *Cell Reports Methods* **2021**, *1* (1). https://doi.org/10.1016/j.crmeth.2021.100009.

(40) Ehrlich, R.; Wulf, V.; Hendler-Neumark, A.; Kagan, B.; Bisker, G. Super-Resolution Radial Fluctuations (SRRF) Nanoscopy in the near Infrared. *Opt. Express* **2022**, *30* (2), 1130. https://doi.org/10.1364/oe.440441.

(41) Kagan, B.; Hendler-Neumark, A.; Wulf, V.; Kamber, D.; Ehrlich, R.; Bisker, G. Super-Resolution Near-Infrared Fluorescence Microscopy of Single-Walled Carbon Using Deep Learning. *Adv. photonics Res.* **2022**, *3* (2200244). https://doi.org/10.1002/adpr.202200244.

(42) Ai, N.; Walden-Newman, W.; Song, Q.; Kalliakos, S.; Strauf, S. Suppression of Blinking and Enhanced Exciton Emission from Individual Carbon Nanotubes. *ACS Nano* **2011**, *5* (4), 2664–2670. https://doi.org/10.1021/nn102885p.

(43) Hartmann, N. F.; Yalcin, S. E.; Adamska, L.; Hároz, E. H.; Ma, X.; Tretiak, S.; Htoon, H.; Doorn, S. K. Photoluminescence Imaging of Solitary Dopant Sites in Covalently Doped Single-Wall Carbon Nanotubes. *Nanoscale* **2015**, *7* (48), 20521–20530. https://doi.org/10.1039/c5nr06343d.

(44) Danné, N.; Godin, A. G.; Gao, Z.; Varela, J. A.; Groc, L.; Lounis, B.; Cognet, L. Comparative

Analysis of Photoluminescence and Upconversion Emission from Individual Carbon Nanotubes for Bioimaging Applications. *ACS Photonics* **2018**, *5* (2), 359–364. https://doi.org/10.1021/acsphotonics.7b01311.

(45) Culley, S.; Albrecht, D.; Jacobs, C.; Pereira, P. M.; Mercer, J.; Henriques, R. NanoJ-SQUIRREL: Quantitative Mapping and Minimisation of Super-Resolution Optical Imaging Artefacts. *Nat. Methods* **2018**, *15* (4), 263–266. https://doi.org/10.1038/nmeth.4605.NanoJ-SQUIRREL.

(46) Opstad, I. S.; Acuña, S.; Hernandez, L. E. V.; Cauzzo, J.; Škalko-Basnet, N.; Ahluwalia, B. S.; Agarwal, K. Fluorescence Fluctuations-Based Super-Resolution Microscopy Techniques: An Experimental Comparative Study. **2020**, *2008.09195*. *ArXiv*. https://doi.org/10.48550/arXiv.2008.09195 (accessed August 20, 2020).

(47) Cognet, L.; Tsyboulski, D. A.; Rocha, J.-D. R.; Doyle, C. D.; Tour, J. M.; Weisman, R. B. Stepwise Quenching of Exciton Fluorescence in Carbon Nanotubes by Single-Molecule Reactions. *Science* **2007**, *316* (5830), 1465–1469. https://doi.org/10.1126/science.1141316.

(48) Siitonen, A. J.; Tsyboulski, D. A.; Bachilo, S. M.; Weisman, R. B. Surfactant-Dependent Exciton Mobility in Single-Walled Carbon Nanotubes Studied by Single-Molecule Reactions. *Nano Lett.* **2010**, *10* (5), 1595–1599. https://doi.org/10.1021/nl9039845.

(49) Reinhardt, S. C. M.; Masullo, L. A.; Baudrexel, I.; Steen, P. R.; Kowalewski, R.; Eklund, A. S.; Strauss, S.; Unterauer, E. M.; Schlichthaerle, T.; Strauss, M. T.; Klein, C.; Jungmann, R. Ångström-Resolution Fluorescence Microscopy. *Nature* **2023**, *617* (7962), 711–716. https://doi.org/10.1038/s41586-023-05925-9.

(50) Chen, R.; Tang, X.; Zhao, Y.; Shen, Z.; Zhang, M.; Shen, Y.; Li, T.; Chung, C. H. Y.; Zhang, L.; Wang, J.; Cui, B.; Fei, P.; Guo, Y.; Du, S.; Yao, S. Single-Frame Deep-Learning Super-Resolution Microscopy for Intracellular Dynamics Imaging. *Nat. Commun.* **2023**, *14* (1), 1–17.

https://doi.org/10.1038/s41467-023-38452-2.

(51) Li, H.; Sims, C. M.; Kang, R.; Biedermann, F.; Fagan, J. A.; Flavel, B. S. Isolation of the (6,5) Single-Wall Carbon Nanotube Enantiomers by Surfactant-Assisted Aqueous Two-Phase Extraction. *Carbon N. Y.* **2023**, *204* (December 2022), 475–483. https://doi.org/10.1016/j.carbon.2022.12.071.

(52) Ao, G.; Khripin, C. Y.; Zheng, M. DNA-Controlled Parition of Carbon Nanotubes in Polymer Aqueous Two-Phase Systems. *J. Am. Chem. Soc.* **2014**, *136*, 10383−10392. https://doi.org/10.1021/ja504078b.

(53) Lourakis, M. I. A. *Levmar: Levenberg-Marquardt Nonlinear Least Squares Algorithms in {C}/{C}++*, v2.6 (accessed November 29, 2011); ICS-FORTH: http://www.ics.forth.gr/~lourakis/levmar/, **2004**.

(54) Si, R.; Wang, H.; Wei, L.; Chen, Y.; Wang, Z.; Wei, J. Length-Dependent Performances of Sodium Deoxycholate-Dispersed Single-Walled Carbon Nanotube Thin-Film Transistors. *J. Mater. Res.* **2013**, *28* (7), 1004–1011. https://doi.org/10.1557/jmr.2012.321.

(55) Lambert, B. P.; Kerkhof, H.; Flavel, B. S.; Cognet, L. Morphology Determination of Luminescent Carbon Nanotubes by Analytical Super-Resolution Microscopy Approaches Introduction. **2024**, *xmxrj*. *ChemRxiv*. https://doi.org/10.26434/chemrxiv-2024-xmxrj.